

Quench Dynamics in Holographic First-Order Phase Transition

Qian Chen,^a Yuxuan Liu,^b Yu Tian,^{a,c} Xiaoning Wu,^d and Hongbao Zhang^e

^a*School of Physics, University of Chinese Academy of Sciences, Beijing 100049, China*

^b*Kavli Institute for Theoretical Sciences (KITS), University of Chinese Academy of Sciences, Beijing 100190, China*

^c*Institute of Theoretical Physics, Chinese Academy of Sciences, Beijing 100190, China*

^d*Institute of Mathematics, Chinese Academy of Sciences, Beijing 100190, China*

^e*Department of Physics, Beijing Normal University, Beijing 100875, China*

E-mail: chenqian192@mailsucas.ac.cn, liyuxuan@ucas.ac.cn,
ytian@ucas.ac.cn, wuxn@amss.ac.cn, hongbaozhang@bnu.edu.cn

ABSTRACT: In this work, we study the real-time dynamics of heating a phase-separated state in the holographic model of first-order phase transition. Although the response to the positive quench demonstrates a distinct behavior from that to the negative one, they share three characteristic stages in common. In the first stage, each of the two separated phases is driven to a new higher energy state, with a group of energy peaks or valleys excited around the domain walls, depending on whether the quench is positive or negative. In the second stage, such excitations propagate towards the interior of the high energy phase, meet and pass each other with the amplitude decaying gradually. Finally in the third stage, the system settles down to a new phase-separated state through the long wave hydrodynamics. The effect of the quench strength on the final state of the system is also investigated, where the two critical values of the quench strength are found to distinguish three different classes of final states. For a small quench strength, the final state is still a phase-separated state but with higher energy. For a moderate quench strength, the final state can be a metastable state below the phase transition temperature. While for a large quench strength, the final state can be a thermodynamically preferred state at a higher temperature.

KEYWORDS: Black Holes, AdS-CFT Correspondence, Holography and quark-gluon plasmas

Contents

1	Introduction	1
2	Holographic setup	2
2.1	Holographic model	3
2.2	Phase diagrams	4
3	Nonlinear evolution	5
3.1	Phase separation	6
3.2	Quench dynamics	7
4	Conclusion	12
A	Numerical procedure for static solutions	14
A.1	The Einstein-DeTurck formalism	14
A.2	Asymptotic expansions	15
B	Numerical procedure for dynamic evolution	16
B.1	Evolution algorithm	16
B.2	Boundary conditions	17
B.3	Convergence test	18

1 Introduction

The concept of phase transitions is introduced to characterize the sudden change in the thermodynamic properties of the system. Within the framework of equilibrium physics, the real-time dynamics of phase transitions are approximated by the so-called quasi-static process. However, processes far from equilibrium are ubiquitous in nature, in which the descriptions of the thermodynamics and even the hydrodynamics will generally break down. Thus a more realistic fashion is necessary to formulate a theoretical framework to implement the real-time dynamics of phase transitions. Gratefully, holography provides us such a desirable framework, in which a many-body system is mapped into the a few-body gravitational entity with one extra dimension [1–4]. In particular, the real-time dynamics of the many-body system can be extracted from the corresponding bulk dynamics, which is always amenable to the numerical simulations even though the analytic treatment is inapplicable [5].

Among others, such a holographic tool has recently demonstrated its unique power in investigating a variety of issues related to the first-order phase transition, from the thermodynamic properties [6, 7], linear response analysis [8, 9], all the way to the fully

nonlinear evolution simulations [10–21]. In particular, the real-time process of the phase separation via the spinodal decomposition is successfully captured by the bulk gravitational dynamics [12–16]. Although these achievements demonstrate theoretical importance for studying first-order phase transitions, the state itself in the spinodal region is so unstable that it is extremely hard to observe experimentally. Instead, as best exemplified by the process of liquid water freezing, a more realistic manner to implement the phase separation is to inject a seed nucleus into a supercooled state, which serves virtually as the physical process version of the first-order phase transition. This dynamical process exhibits a wealth of critical phenomena [17, 19, 21], analogs to the type I critical gravitational collapse [22–25] and the bald/scalarize black hole transition via a nonlinear accretion of the scalar field [26–28].

Whether starting from the spinodal region or the supercooled region to the final phase separation, the current discussions are basically restricted to microcanonical ensembles, where the energy of the system is conserved throughout the evolution. However, due to interactions with the environment, the energy of the system will almost inevitably be altered during evolution.

In this paper, we elaborate on a broad class of effects of the environment on the system by heating. For a system prepared in the phase separation state, heating may not change its temperature due to the latent heat of the first-order phase transition. However, arising from the interactions between the physical system and the environment, the corresponding dynamical process from the dual gravitational simulations becomes difficult to manipulate. We tend to take up this challenge and manage to investigate the dynamical behavior of the system during a quench process by performing fully nonlinear numerical simulations with the characteristic formulation [5].

The plan of the paper is as follows. After the introduction at section 1, we give a brief description of a holographic first-order phase transition model in section 2, where the Ward-Takahashi identity and phase structure are revealed. In section 3, we present the results of numerical simulations. First, we review the physical process of the system reaching the phase-separated state from the spinodal region and the supercooled region, respectively. Next, we take the phase-separated state as the initial data and then impose a time-dependent quench to it. The three characteristic stages that the system undergoes in the quench process are revealed. Finally, we conclude the paper by a summary and an outlook in section 4.

2 Holographic setup

In this section, we will introduce a holographic model with a first-order phase transition, and then show the Ward-Takahashi identity and phase structure.

2.1 Holographic model

We consider the Einstein-Scalar system in the four-dimensional asymptotically anti-de Sitter spacetime described by the Lagrangian density

$$\mathcal{L} = R - \frac{1}{2}\nabla_\mu\phi\nabla^\mu\phi - V(\phi), \quad (2.1)$$

with scalar potential

$$V(\phi) = -6\cosh\left(\frac{\phi}{3}\right) - \frac{\phi^2}{5}, \quad (2.2)$$

where the AdS scale has been chosen to be $L = 1$ for convenience. According to the AdS/CFT correspondence, such a gravity system corresponds to a boundary conformal field theory with a scalar operator of conformal dimension $\Delta = 2$. In order to explore the energy-momentum tensor operator and scalar operator, we are required to renormalize the bulk action to make it finite by adding some following boundary terms [29–31]

$$2\kappa_4^2 S_{\text{ren}} = \int_M dx^4 \sqrt{-g} \mathcal{L} + 2 \int_{\partial M} dx^3 \sqrt{-\gamma} K - \int_{\partial M} dx^3 \sqrt{-\gamma} \left(R[\gamma] + 4 + \frac{1}{2}\phi^2 \right), \quad (2.3)$$

where $R[\gamma]$ is the Ricci scalar associated with the induced metric $\gamma_{\mu\nu}$ on the boundary and K is the trace of extrinsic curvature $K_{\mu\nu} = \gamma_\mu^\sigma \nabla_\sigma n_\nu$ with n_ν the outward normal vector field to the boundary. On the one hand, the variation of this renormalized action with respect to the bulk fields gives rise to the field equations

$$R_{\mu\nu} - \frac{1}{2}Rg_{\mu\nu} = \frac{1}{2}\nabla_\mu\phi\nabla_\nu\phi - \left(\frac{1}{4}(\nabla\phi)^2 + \frac{1}{2}V(\phi) \right) g_{\mu\nu}, \quad (2.4a)$$

$$\nabla^\mu\nabla_\mu\phi = \frac{dV(\phi)}{d\phi}. \quad (2.4b)$$

On the other hand, by definition, the above two dual operators have the form

$$\langle O \rangle = \kappa_4^2 \lim_{r \rightarrow \infty} \frac{r^2}{\sqrt{\gamma}} \frac{\delta S_{\text{ren}}}{\delta \phi} = -\frac{1}{2} \lim_{r \rightarrow \infty} r^2 (\phi + n^\mu \nabla_\mu \phi), \quad (2.5a)$$

$$\langle T_{ij} \rangle = -2\kappa_4^2 \lim_{r \rightarrow \infty} \frac{r}{\sqrt{\gamma}} \frac{\delta S_{\text{ren}}}{\delta \gamma^{ij}} = \lim_{r \rightarrow \infty} r \left[G[\gamma]_{ij} - K_{ij} - \left(2 - K + \frac{1}{4}\phi^2 \right) \gamma_{ij} \right]. \quad (2.5b)$$

For their specific expressions in this work, we refer readers to Appendix B. Then the variation of the renormalized on-shell action gives rise to

$$\kappa_4^2 \delta S_{\text{ren}} = \int_{\partial M} d^3x \sqrt{-\gamma_{(0)}} \left(-\frac{1}{2} \langle T_{ij} \rangle \delta \gamma_{(0)}^{ij} + \langle O \rangle \delta \phi_{(0)} \right), \quad (2.6)$$

where the subscripts denote the coefficients of the leading order term in the asymptotic behavior at the boundary.

Such a renormalized on-shell action keeps the diffeomorphism invariance

$$\delta \gamma^{ij} = \mathcal{L}_\xi \gamma^{ij}, \quad \delta A_i = \mathcal{L}_\xi A_i, \quad \delta \psi = \mathcal{L}_\xi \psi, \quad (2.7)$$

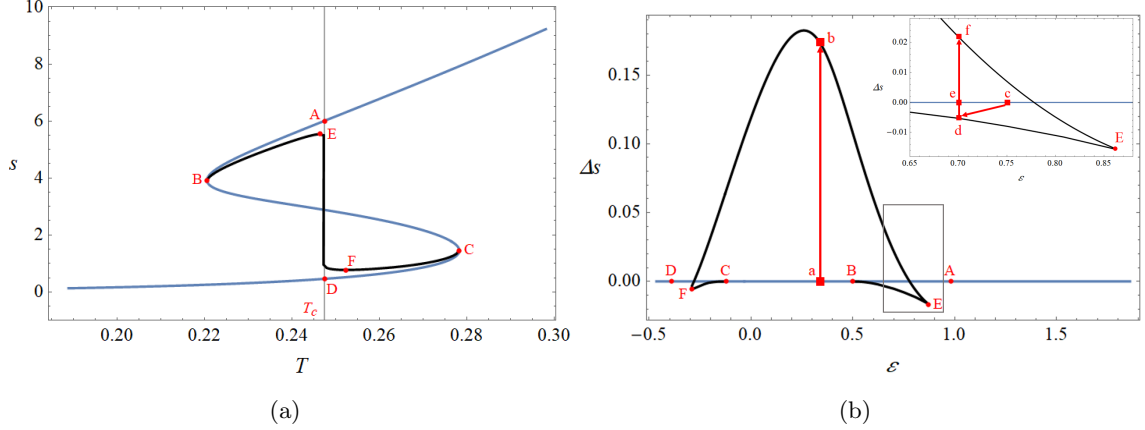


Figure 1. Canonical phase diagram (a): the entropy density as a function of the temperature. Note that the points E and F cannot respectively coincide with points A and D due to the effect of spatial size [17]. Microcanonical phase diagram (b): the entropy density difference between the inhomogeneous and homogeneous states as a function of the energy density. The blue and black lines represent homogeneous and inhomogeneous states, respectively. The vertical gray line represents the phase transition temperature. The schematic paths (a, b) and (c, d, f) correspond to the dynamic processes shown in the upper and lower panels of Fig. 2, respectively.

where \mathcal{L}_ξ is the Lie derivative with respect to an arbitrary vector field ξ^i tangent to the boundary. Therefore we can derive the Ward-Takahashi identity as follows

$$\nabla^j \langle T_{ij} \rangle = \langle O \rangle \nabla_i \phi_{(0)}, \quad (2.8)$$

which indicates the time-dependent scalar source induces the change in the energy

$$\partial_t \epsilon - \partial_x J_x = - \langle O \rangle \partial_t \phi_{(0)}, \quad (2.9)$$

where symbols ϵ and J_x represent the energy density and momentum density in the x -direction, respectively. The main purpose of this work is to reveal the fully nonlinear evolution of the system in the phase-separated state with a time-dependent scalar source.

2.2 Phase diagrams

In order to reveal the phase structure of this model, we numerically seek out the static solutions to the field equations (2.4) using the Deturk method [32] and the nonlinear evolution method [5]. The procedures of these methods are described in Appendix A and Appendix B, respectively. As the geometry has been determined, we can extract the physical quantities of the system and display them in Fig. 1.

The equation of states of the system is shown in Fig. 1(a) as the temperature dependence of the entropy density. The blue and black lines represent homogeneous and inhomogeneous states, respectively. On the one hand, based on the stability of the system, the homogeneous states can be divided into three types. First, the thermodynamically preferred phases lying on the upper and lower branch with entropy density above that of

point A and below that of point D are stable [8]. They are discontinuous at the temperature $T_c = 0.247$ indicating the gauge theory possesses a thermal first-order phase transition in the canonical ensemble. Second, the metastable states in the AB and CD regions are linearly stable but nonlinearly unstable. To trigger the dynamical transition, they are required to cross a critical state as the dynamical barrier [17, 21]. Third, the spinodal region between points B and C is linearly unstable, meaning that the dynamical transition can occur with arbitrarily small perturbation [13]. On the other hand, the inhomogeneous states can be classified into two categories according to their stability. The states with a single unstable mode in the BE and CF regions are exactly the critical states required for the metastable state to undergo a dynamical transition. The last remaining phase-separated states in the EF region are the final states in the dynamical transition process. The different spatial regions of these states are occupied by the different phases at the phase transition temperature (the phases at points A and D), and joined by a domain wall.

In order to discuss the two kinds of dynamical transition mechanisms mentioned above more clearly, we draw the microcanonical phase diagram in Fig. 1(b) as an energy density dependence of the entropy density difference between the inhomogeneous and homogeneous states. In the microcanonical ensemble, the system tends to be in the state of maximum entropy. Due to the spinodal instability in the BC region, the system in the state at point a will spontaneously evolve to the phase-separated state at point b with greater entropy but the same energy. However, there is a different story for the states in AB and CD regions. Without loss of generality, we take the state at point c as an example. At this point, the system is stable under small perturbations. A quench of sufficient strength is required as a seed nucleus to trigger the dynamical transition. Moreover, if the quench strength approaches a threshold, the system exhibits a critical behavior. This process can be divided into three stages. First, with the addition of the seed nucleus, the energy and entropy of the system suddenly decrease. Then, the system sharply converges to a critical state at point d . Finally, the phase-separated state with maximum entropy at point f is reached for supercritical strength, and conversely, the system evolves to the homogeneous state with local maximum entropy at point e [21]. The details of the real-time dynamics during the dynamical transition are presented in Fig. 2, which we will describe in the next section.

3 Nonlinear evolution

In this section, we show the fully nonlinear numerical simulations of the dual gravitational dynamics. The system of equations (2.4) is solved numerically to reveal the processes of dynamical transition and heating, which occur under the reflecting boundary conditions and time-dependent scalar source boundary conditions, respectively. For more details on the numerical procedure, we refer readers to Appendix B, and the code is freely available at <https://github.com/QianChen2022/HFOPT>.

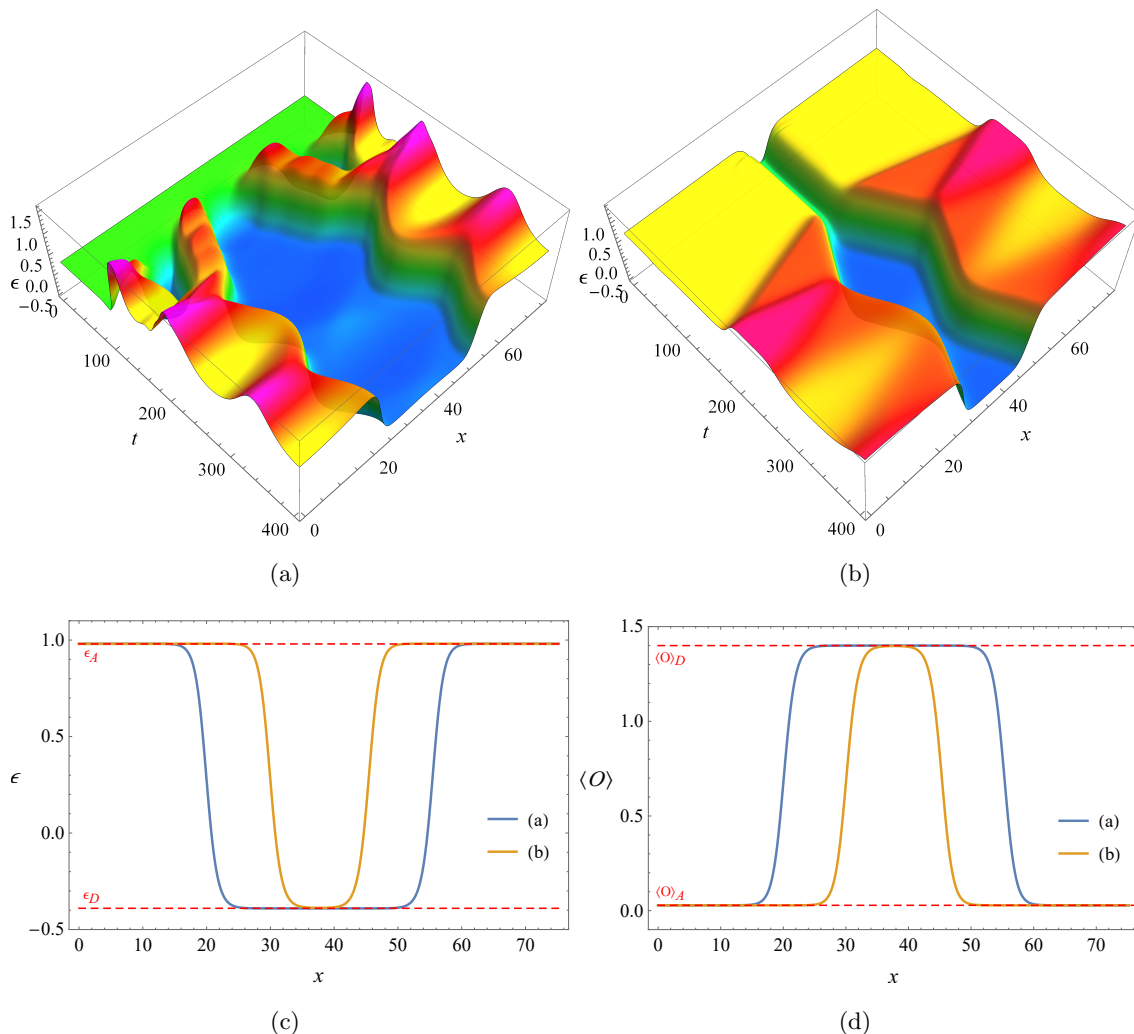


Figure 2. (a, b): The energy density as a function of time with the initial states at points a in the spinodal region and c in the supercooled region in Fig. 1(b), respectively. (c, d): The spatial dependence of the energy density and expectation value of the scalar field of the final state. The blue and orange lines correspond to the final states given in the processes (a) and (b), respectively. The horizontal red dotted lines represent the states at the phase transition temperature in homogeneous solutions (points A and D in Fig. 1(b)). Note that the high-energy phase has a lower expectation value of the scalar field, while the low-energy phase possesses a higher one.

3.1 Phase separation

In this subsection, we construct the phase-separated state as the initial data for the heating process. Without loss of generality, we choose the states at points a in the spinodal region and c in the supercooled region in Fig. 1(b) as the initial states to reveal the two dynamical transition mechanisms. The real-time dynamics of these two dynamical transitions are shown in Fig. 2(a) and Fig. 2(b), respectively.

For the case of spontaneous dynamical transition, since the initial state suffers from

the spinodal instability, arbitrarily small perturbations will trigger the system to undergo a dynamical transition. Therefore, we impose an x -dependent perturbation of the following form on the scalar field

$$\delta\phi = -0.1z^2(1-z)^2\exp[-10\cos^2(x/24)]. \quad (3.1)$$

As we can see from Fig. 2(a), such a form of perturbation excites three energy peaks on the background of the homogeneous solution. Note that the peaks on both sides of the space are actually the same due to the periodic boundary condition. Then, two of the energy peaks move slowly toward the other. They subsequently collide and merge together, forming a larger phase. Eventually, the system gradually settles down to a phase-separated state shown in Fig. 2(c) and Fig. 2(d). It consists of the phases at points A and D in Fig. 1(b), and these different phases are connected by domain walls.

However, in the case of dynamical transition from the supercooled region, the system is stable under small perturbations, meaning that the states in this region have no unstable modes [8]. The occurrence of the dynamical transition requires a perturbation large enough to quench the system over a dynamical barrier. So, we add a disturbance of sufficiently large amplitude served as seed nucleus to the system

$$\delta\phi = pz^2\exp[-50\cot^2(x/24)], \quad (3.2)$$

with $p = 1.285364$. As we can see from Fig. 2(b), at early times, the system is quickly attracted to a critical state at point d in Fig. 1(b) and remains there for a long time. Then, the nucleus gradually grows to form the low-energy phase. Finally, the phase-separated state is reached. Since the energy of the system, in this case, is higher than that of the spontaneous dynamical transition, the ratio of the space occupied by the high-energy phase and the low-energy phase of its final state is naturally larger than that of the spontaneous dynamical transition, which is shown in Fig. 2(c) and Fig. 2(d). Actually, during this process, the system exhibits critical behavior similar to the type I critical gravitational collapse [25] and the bald/scalarize black hole transition [26]. That is to say, there is a threshold p_* such that the system just stays on the critical state. For supercritical parameter $p > p_*$, the dynamical transition occurs, and instead, the system returns to a homogeneous state. Moreover, for p near p_* , the system will be attracted to the critical state and stay there for a period of time satisfying

$$\tau \propto -\gamma\ln(|p - p_*|), \quad (3.3)$$

where the critical exponent γ is equal to the reciprocal of the eigenvalue of the only unstable eigenmode of the critical state. For more details, please refer to [21].

3.2 Quench dynamics

Based on the results of the phase separation, we will further investigate the nonlinear dynamics for time-dependent scalar source on the background solution of the phase-separated state in this subsection. Since the confining AdS boundary prohibits matter escaping, the

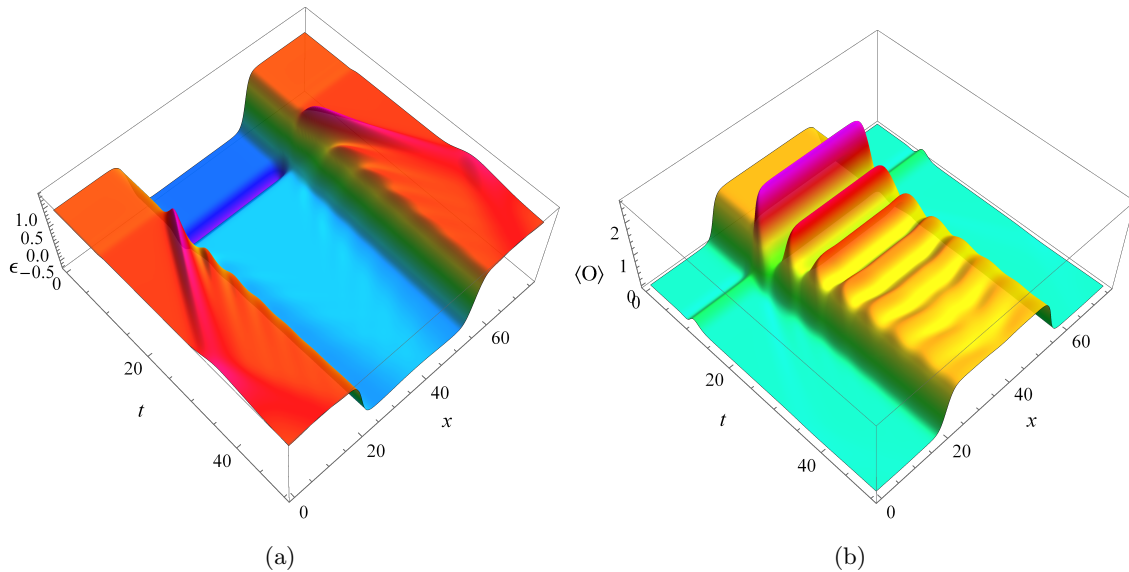


Figure 3. The temporal and spatial dependence of the energy density (a) and the expectation value of scalar field (b) in the quench process with quench strength $H = 0.2$.

above two dynamical transition processes essentially occur under the microcanonical ensemble as the total energy of the system is conserved during the evolution. However, as we can see from the Ward-Takahashi identity (2.8), the time-dependent scalar source can induce the change in the total energy as follows

$$\partial_t E = - \int dx \langle O \rangle \partial_t \phi_{(0)}. \quad (3.4)$$

Note that the periodic boundary conditions are imposed in the spatial x -direction. Actually, in addition to the energy, the electric charge of a charged system changes as well under the time-dependent scalar source boundary conditions [33–35].

In order to reveal the response of the system to the scalar source, we specify a time dependency to the scalar source on the phase-separated state obtained from the process in Fig. 2(a) as follows

$$\phi_{(0)} = \Lambda + H \exp \left[-0.5 (t - 10)^2 \right], \quad (3.5)$$

where the parameter H is the strength of the quench and the source decays rapidly to the constant Λ at late times, which is the boundary condition for the dynamical transition processes and is set to 1 in our work. The real-time dynamics during the quench process with strength $H = 0.2$ are shown in Fig. 3. The overall evolution process can be divided into three characteristic stages. In the first stage, the variation in energy density is dominated by a combination of the time-dependent scalar source and the expectation value of the scalar field. There is no energy flow in the space region occupied by the two phases, resulting in the phenomenon that the energy density can only be shifted up and down shown in Fig. 4(a). This stage is a process in which the two phases are each quenched independently. Since the low-energy phase possesses a larger expectation value, its energy

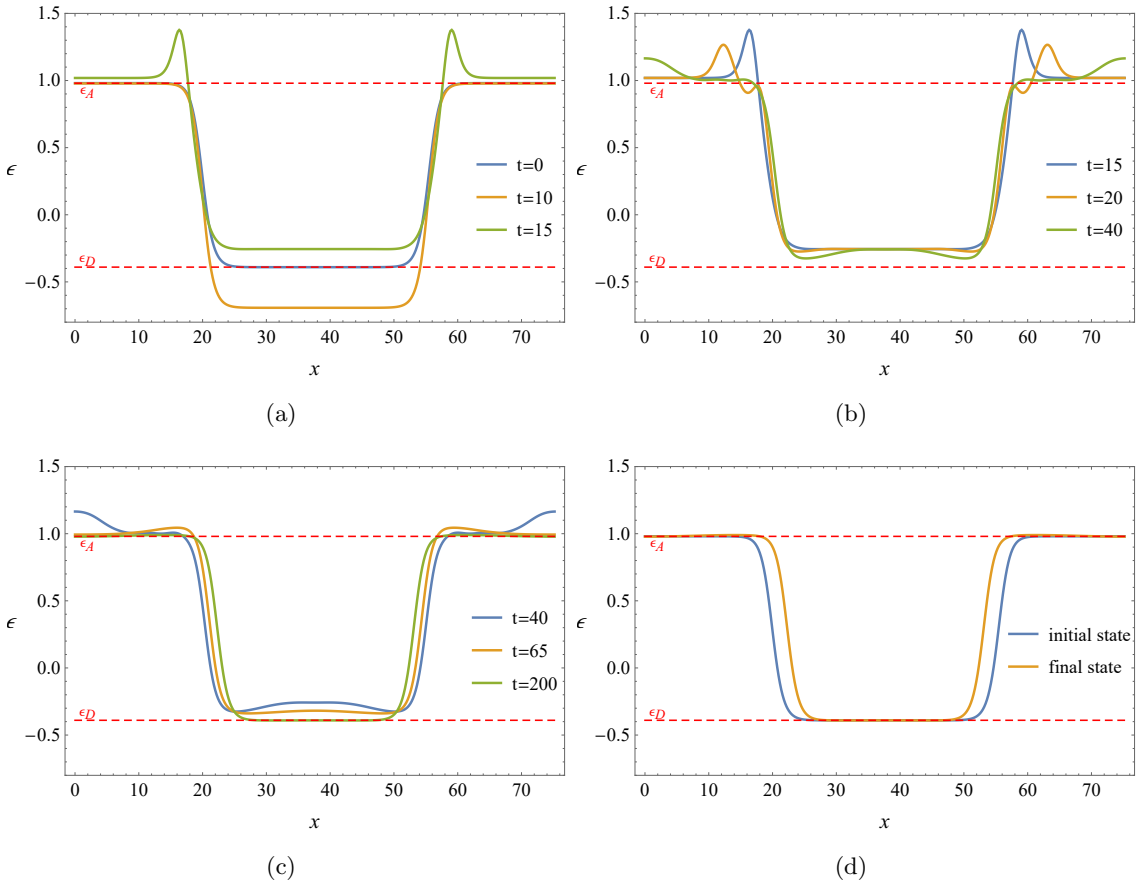


Figure 4. (a,b,c): Three characteristic stages in the quench process. The solid lines of different colors represent the energy density of the system at different times. The horizontal red dotted lines represent the energy density of the states at the phase transition temperature in homogeneous solutions. (d): The energy density of the initial and final states during the quench process.

density is more sensitive to the response of the scalar source, which can be easily seen from (2.9). When $t < 10$, the energy density of the low-energy phase decreases synchronously as the source increases due to the positive expectation value. However, the energy density of the high-energy phase hardly changes during this period as its expectation value is close to 0. When $10 < t < 15$, as the source decays to its initial value Λ , the energy density curves of both phases rise and stabilize at a new location where the energy density is higher than the initial value. That is to say, after the quench, the energy of both the low-energy phase and the high-energy phase is increased. This is a stage in which the total energy of the system varies with the scalar source. After this, the total energy is conserved since the scalar source is a constant, as shown in Fig. 5(a). An intriguing phenomenon at the end of the first stage is the behavior of the domain walls. Two energy peaks are excited at the junctions of domain walls and the high-energy phase. And in the second stage shown in Fig. 4(b), the energy peaks propagate towards the interior of the high energy phase. At late times, they collide at the center of the phase domain and merge together. At time

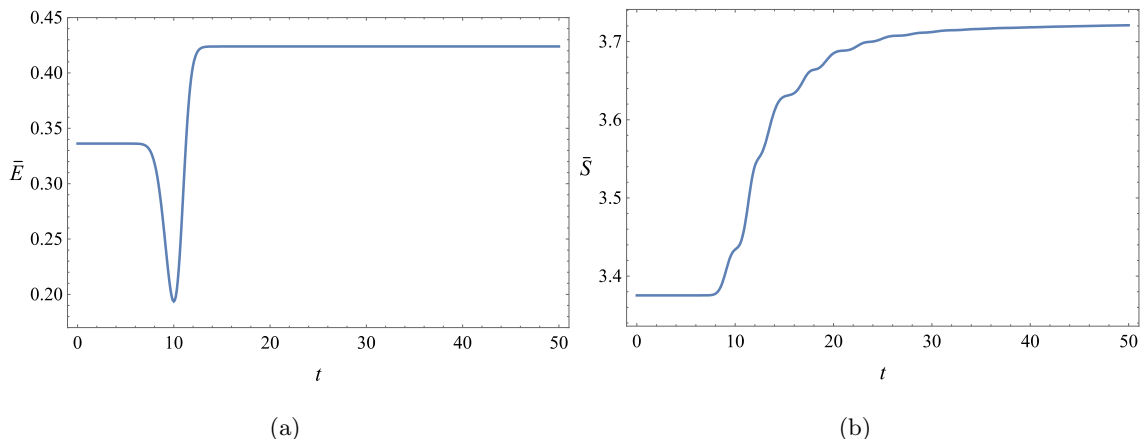


Figure 5. The average energy (a) and the average entropy (b) of the system as a function of time during quenching with $H = 0.2$.

$t = 20$, the second set of energy peaks are excited again at the domain walls and then move outward. They will subsequently be absorbed by the first set of energy peaks. During this stage, multiple groups of energy peaks propagating outward are excited successively at the domain walls, which are shown as sawtooth-like ripples in Fig. 3(a). They end up merging together to form a larger one at time $t = 40$. Finally, in the third stage shown in Fig. 4(c), the energy peak splits into two inward propagating energy waves. They then hit the domain walls with the result that part of them goes through and the other part bounces off. As the energy waves repeatedly propagate through space and gradually decay, the system eventually converges to a phase-separated state with the same properties as the initial state but with a larger total energy shown in Fig. 4(d). During the quench process, the expectation value of the scalar field mainly exhibits oscillatory behavior shown in Fig. 3(b).

The time dependence of the average energy and average entropy defined as $\bar{S} = \frac{2\pi}{L_x} \int dx \Sigma^2(r_h)$ in the quench process are shown in Fig. 5, where $\Sigma^2(r_h)$ represents the area of the apparent horizon and L_x stands for the length of the box. Since the integral of the expectation value of the scalar field is always positive, the monotonicity of the change in energy is just the opposite of that of the scalar source shown in Fig. 5(a), which is easily seen from (3.4). Although the energy can increase or decrease during the quench process, the energy of the final state is always higher than that of the initial state. The reason for this is that, on the one hand, the changes in the physical quantities of the initial and final states satisfy the following first law of black hole thermodynamics

$$\Delta E = T_c \Delta S. \quad (3.6)$$

Note that T_c is the phase transition temperature, which is also the temperature of the initial and final states of the system during the quench process. And on the other hand, the second law of black hole mechanics requires the entropy of the system never decreases

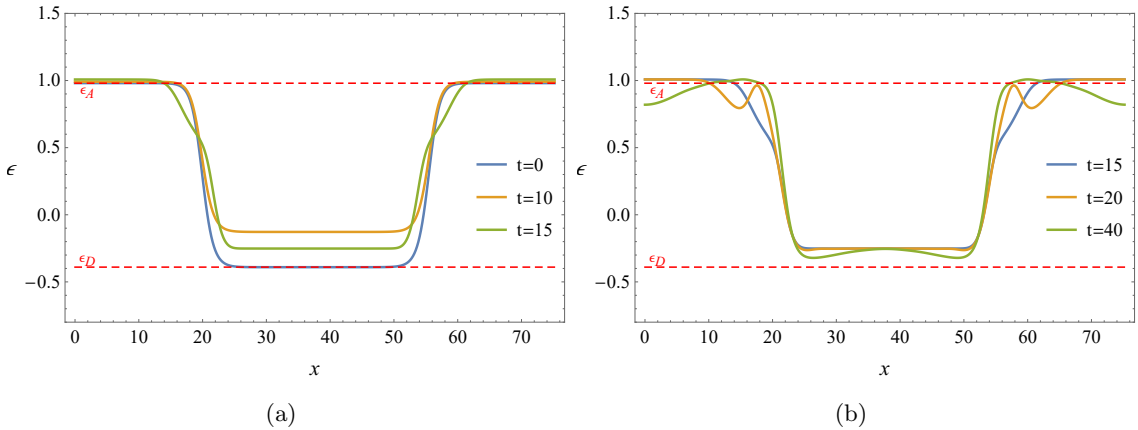


Figure 6. The first (a) and second (b) stages in the quench process with quench strength $H = -0.2$.

in dynamical processes, which is shown in Fig. 5(b). Therefore, the right-hand side of the above equation is always positive, indicating that the energy of the system cannot be extracted through the quench process. This is different from the charged system [33–35].

There is a similar but different phenomenon for the case where quench strength H is negative. The first and second stages of this dynamic process with $H = -0.2$ are shown in Fig. 6. Since the third stage is the stage where the system is in the linear region of the phase-separated state similar to the process in Fig. 4(c), we only focus on the dynamical behavior of the system in the first two stages here. As we can see from Fig. 6(a), in the first stage, the variation of the energy density in the two-phase region is similar to Fig. 4(a), which translates up and down as the scalar source is turned on and off. Since the monotonicity of the variation of the scalar source is opposite to the situation where H is positive, the up and down motion of the energy curve is also reversed. However, the fundamental difference is the dynamical behavior of the domain walls. There are no energy peaks excited, instead, the position of domain walls changes significantly. The configuration of domain walls is broken at some point in the middle, then the top half expands and the bottom half contracts. As we can see from the second stage shown in Fig. 6(b), domain walls in the upper half gradually evolve into a set of energy valleys propagating outward. Finally, they collide in the middle of the region occupied by the high-energy phase and merge together. Actually, at this stage, multiple groups of energy valleys are generated from the domain walls and are absorbed one by one, similar to the phenomenon in Fig. 4(b).

In order to further reveal the effect of quench strength on the system, we draw the variation of the average energy of the final state with the quench strength in Fig. 7(a). We find that the stronger the quench, the more energy it brings to the system. Moreover, the quench with sufficient strength (greater than the critical value H_*) will destroy the phase-separated structure and drive the system to a homogeneous final state. Interestingly, the final state of the quench process with strength $H_* < H < H_A$ shown in Fig. 7(b) is not the thermodynamically preferred state, but a metastable state in the supercooled region with

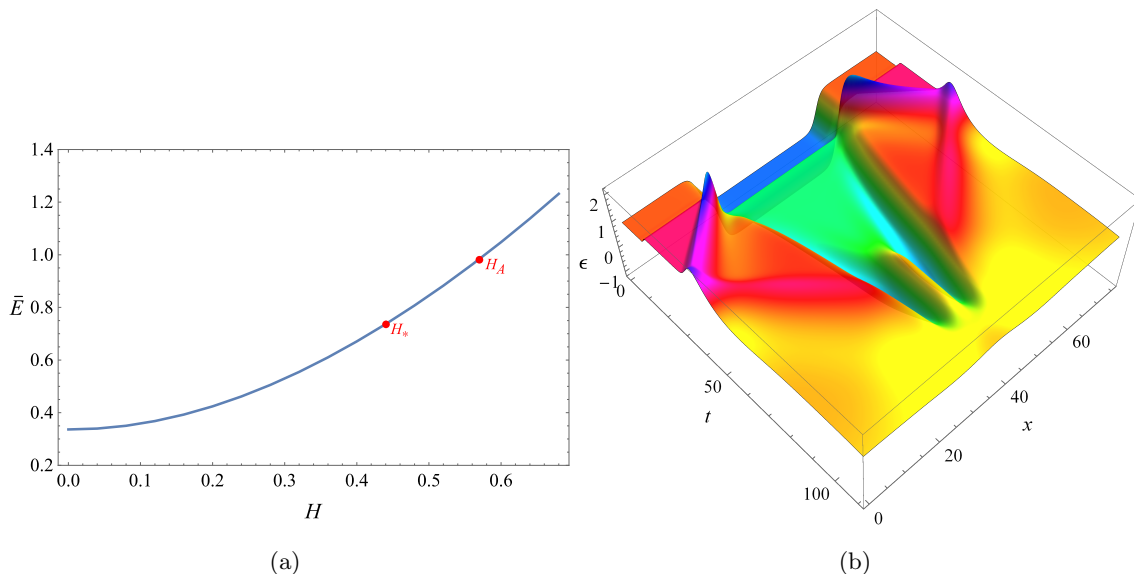


Figure 7. (a): The average energy of the final state of the quench process as a function of quench strength. When the quench strength is larger than the critical value H_* , the final state is a homogeneous state, on the contrary, it is still a phase-separated state. The final state of the quench process with strength $H_A < H$ lie on the upper branch with energy above that of point A in Fig. 1(a). That is to say, the final state is a supercooled state in the AB region of Fig. 1(a) when the quench strength $H_* < H < H_A$. (b): The energy density as a function of time during the quench process with a strength slightly greater than the critical quench strength H_* .

nonlinear instability. This indicates that the system can undergo a dynamical transition to the phase-separated state again by adding a seed nucleus similar to the process in Fig. 2(b). However, when the quench strength $H_A < H$, the system is quenched to a stable homogeneous state lying on the upper branch with energy above that of point A in Fig. 1(a). The results also show that although such quench process always increases the energy of the system, the temperature of the final state can remain unchanged, decrease or increase, depending on the quench strength.

4 Conclusion

In this paper, we have investigated the quench dynamics in the holographic model of first-order phase transition, via the characteristic formalism. Specifically, we have heat an phase-separated initial state, and subsequently tracked its non-linearly dynamical evolution.

In the first step, the phase-separated initial state is prepared by adopting different strategies. For a low-energy initial state, it has been prepared by perturbing an unstable state in the spinodal region. Due to the linear instability, any arbitrarily small perturbation will drive the system to phase separation. While a high-energy initial state has been prepared by perturbing a metastable state, which suffers from nonlinear instability. In

these cases, the dynamical transition can still be triggered by applying a sufficiently strong disturbance that served as a seed nucleus to the system.

In the second step, we studied the dynamical behavior of the system on such a phase-separated state in the case of temporal dependence of the scalar source, by turning on a thermal quench in a short period of time. We have found that there are two distinct forms of response to the quenches with different signs. And the system exhibits three characteristic stages in each response process. The first stage can be seen as a process in which the high-energy and low-energy phases are quenched independently, since no energy flow has been formed in the whole space. As we can see from the Ward-Takahashi identity (2.9), the time-dependent scalar source affects the energy of the system through the expectation value of the scalar field. Due to the positive expectation value possessed by the low-energy phase, the monotonicity of its energy over time is just the opposite of that of the scalar source. Naturally, the quenches of different signs will induce the energy to vary in opposite ways with time. However, for the high-energy phase, the energy hardly changes because of the almost vanishing expectation value of the scalar field. At the end of this stage, the interesting thing is the dynamical behavior of the domain walls, which exhibit different responses to the quenches with different signs. For the quench with plus (minus), there are two energy peaks (valleys) excited at the domain walls. Subsequently, in the second stage, they propagate deep into the high-energy phase region. During the process, multiple groups of energy peaks or valleys are excited and absorbed successively, forming a large energy flow. Finally for weakly quench strength, as the energy flow decays in space, the system gradually settles down to a phase-separated state with greater energy in the third stage.

Moreover, the change in the quench strength will generally lead to a change in the final state. As the quench strength increases, we found there is a critical value of strength H_* that can break the phase-separated structure and dynamically drive the system to a homogeneous state. As we can see from the microcanonical phase diagram in Fig. 1(b), there are two possibilities for the homogeneous state with energy greater than the phase-separated state at point b : the metastable state in the AB region and the stable state with higher energy than the state at point A . Note that the system can not stay in the state with an energy lower than the state at point B due to the spinodal instability. The results in Fig. 7(a) indicate that there is a second critical value of strength H_A . When the quench strength $H_* < H < H_A$, the system evolves into the metastable state below the phase transition temperature. While in the case where $H_A < H$, the final state is in a thermodynamically stable phase.

In the future, it is interesting to explore the effect of the topology on the boundary system. Due to the periodic boundary condition along x direction, the system is located on a torus. The aperiodic boundary condition is introduced in AdS/BCFT duality [36, 37], or more recently, the double holography [38–40]. For the numerical setups in higher dimensions [41–44], CFL conditions may have more stringent constraints on aperiodic boundary conditions. Furthermore, to study the properties of strongly coupled quantum systems near phase transition points [45–49], one can observe the changes in entanglement entropy [50–53] and complexity [54–57] during the quench process [34, 58–66]. It would be aslo

interesting to extend our analysis to some other gravity modes, such as the charged inhomogeneous system. In addition, it is meaningful to seek a hydrodynamic description for the quench process.

A Numerical procedure for static solutions

A.1 The Einstein-DeTurck formalism

The line element of the standard Schwarzschild-AdS₄ geometry is

$$ds^2 = \frac{1}{z^2} \left[-f(z)dt^2 + \frac{dz^2}{f(z)} + dx^2 + dx_1^2 \right], \quad (\text{A.1})$$

$$f(z) = 1 - \left(\frac{z}{z_h} \right)^3, \quad (\text{A.2})$$

where $z = z_h$ is the locus of the bifurcation and the AdS radius L has been set to 1. For a regular metric on the bifurcation, the transformation of radial coordinate z is imposed to be

$$y = \sqrt{1 - \frac{z}{z_h}},$$

which renders the conformal boundary to be $y = 1$ and locus of the bifurcation to be $y = 0$. With the break of the translational symmetry along x direction, the most general metric reads

$$ds^2 = \frac{1}{z_h^2(1-y^2)^2} \left[-y^2 P Q_1 dt^2 + \frac{4z_h^2 Q_2}{P} dy^2 + Q_4 (dx + y(1-y)^3 Q_3 dy)^2 + Q_5 dx_1^2 \right], \quad (\text{A.3})$$

$$\phi = z_h(1-y^2) Q_6, \quad (\text{A.4})$$

with $P = 3 - 3y^2 + y^4$ and Q_i ($i = 1, \dots, 6$) being the functions of (x, y) .

Instead of solving Einstein equations (2.4) directly, we solve the so-called Einstein-DeTurck equations, which are

$$R_{\mu\nu} + 3g_{\mu\nu} = \left(T_{\mu\nu} - \frac{T}{2} g_{\mu\nu} \right) + \nabla_{(\mu} \xi_{\nu)}, \quad (\text{A.5})$$

where

$$\xi^\mu := [\Gamma_{\nu\sigma}^\mu(g) - \Gamma_{\nu\sigma}^\mu(\bar{g})] g^{\nu\sigma}$$

is the DeTurck vector and \bar{g} is the reference metric, whose line element is chosen to be (A.1). For Dirichlet boundaries, \bar{g} is required to satisfy the same boundary conditions as g , but there is no requirement on Neumann boundaries [41] (see also in [42, 44]).

The domain of interest is periodic in x direction, which is $x \in [0, 2l]$. Considering the mirror symmetry at $x = l$, the whole domain of integration can be reduced to $x \in [0, l]$ together with $y \in [0, 1]$. The full boundary conditions are shown in Tab. 1.

Due to the non-periodicity, both directions are discretized by the Chebyshev Pseudo-spectral method with Gauss-Lobatto grids. Subsequently, the geometry can be solved numerically by the Newton-Raphson iteration.

	1	2	3	4	5	6
$\mathbf{y} = \mathbf{1}$	$Q_1 = 1$	$Q_2 = 1$	$Q_3 = 0$	$Q_4 = 1$	$Q_5 = 1$	$Q_6 = 1$
$\mathbf{y} = \mathbf{0}$	$\partial_y Q_1 = 0$	$\partial_y Q_2 = 0$	$\partial_y Q_3 = 0$	$\partial_y Q_4 = 0$	$\partial_y Q_5 = 0$	$\partial_y Q_6 = 0$
$\mathbf{x} = \mathbf{1}$	$\partial_x Q_1 = 0$	$\partial_x Q_2 = 0$	$Q_3 = 0$	$\partial_x Q_4 = 0$	$\partial_x Q_5 = 0$	$\partial_x Q_6 = 0$
$\mathbf{x} = \mathbf{0}$	$\partial_x Q_1 = 0$	$\partial_x Q_2 = 0$	$Q_3 = 0$	$\partial_x Q_4 = 0$	$\partial_x Q_5 = 0$	$\partial_x Q_6 = 0$

Table 1. Boundary conditions.

The boundary conditions at the bifurcation $y = 0$ will further imply that $Q_1(x, 0) = Q_2(x, 0)$, which fixes the Hawking temperature of the black hole as

$$T_h = \frac{3}{4\pi z_h}. \quad (\text{A.6})$$

A.2 Asymptotic expansions

In the Fefferman-Graham expansion of $\{Z, \chi\}$, the asymptotic behaviors of Q_i near the conformal boundary $Z = 0$ are obtained as

$$Q_1 = 1 - \frac{Z^2}{8} - \frac{Z^3 \left(3z_h^2 + Q_1^{(0,3)}[\chi, 1] \right)}{48z_h^3} + \dots, \quad (\text{A.7})$$

$$Q_2 = 1 - \frac{Z^3 Q_6^{(0,1)}[\chi, 1]}{6z_h} + \dots, \quad (\text{A.8})$$

$$Q_3 = -\frac{Z Q_3^{(0,1)}[\chi, 1]}{2z_h} + \frac{Z^2 \left(-Q_3^{(0,1)}[\chi, 1] + Q_3^{(0,2)}[\chi, 1] \right)}{8z_h^2} + \dots, \quad (\text{A.9})$$

$$Q_4 = 1 - \frac{Z^2}{8} - \frac{Z^3 \left(3z_h^2 + Q_4^{(0,3)}[\chi, 1] \right)}{48z_h^3} + \dots, \quad (\text{A.10})$$

$$Q_5 = 1 - \frac{Z^2}{8} + \frac{Z^3 \left(6z_h^2 + 24z_h^2 Q_6^{(0,1)}[\chi, 1] + Q_1^{(0,3)}[\chi, 1] + Q_4^{(0,3)}[\chi, 1] \right)}{48z_h^3} + \dots, \quad (\text{A.11})$$

$$Q_6 = 1 - \frac{Z Q_6^{(0,1)}[\chi, 1]}{2z_h} - \frac{193Z^2}{720} + \dots, \quad (\text{A.12})$$

where the derivatives $Q_i^{(0,j)}$ ($i = \{1, \dots, 6\}$; $j = \{1, 2, 3\}$) are related to coordinate y . For instance, $Q_6^{(0,1)}[\chi, 1]$ means that $Q_6^{(0,1)}[\chi, y] \Big|_{y=1}$.

With these expansions in hand, the entropy and energy density can be expressed by

$$s(\chi) = \frac{2\pi}{z_h^2} \sqrt{Q_4[\chi, 0] Q_5[\chi, 0]}, \quad (\text{A.13})$$

$$e(\chi) = \frac{96 + 9z_h^2 + 32z_h^2 Q_6^{(0,1)}[\chi, 1] + 3Q_1^{(0,3)}[\chi, 1]}{96z_h^3}, \quad (\text{A.14})$$

respectively.

B Numerical procedure for dynamic evolution

B.1 Evolution algorithm

For the nonlinear evolution, the coupled field equations (2.4) are solved numerically using the characteristic formulation method in [5], which has been shown to be applicable to various gravitational dynamics problems in the asymptotically AdS spacetime. The ansatz for the metric is given by

$$ds^2 = \Sigma^2 (Gdx^2 + G^{-1}dy^2) + 2dt (dr - Adt - Fdx), \quad (\text{B.1})$$

where all fields are functions of (t, x, r) . To simplify the problem, we have assumed that the system is translation invariance in the y direction. Note that such form of ansatz is invariance under the radial shifts

$$r \rightarrow \bar{r} = r + \lambda(t, x), \quad (\text{B.2a})$$

$$A \rightarrow \bar{A} = A + \partial_t \lambda(t, x), \quad (\text{B.2b})$$

$$F \rightarrow \bar{F} = F + \partial_x \lambda(t, x), \quad (\text{B.2c})$$

and in general, there are two ways to fix the parameter λ . One simple way is to require λ to disappear throughout the evolution. However, in our work, we use the reparameterization freedom to put the apparent horizon at a fixed radial position. In this case, since the computational domain is a fixed interval, we can conveniently discretize the fields with pseudospectral methods. The Chebyshev and Fourier pseudospectra are used to discretize the fields in the radial (z) and spatial (x) direction, respectively. Note that we compactify the radial coordinate by $z = r^{-1}$ such that the AdS boundary at the position of $z = 0$.

In order to decouple the field equations, we introduce a derivative operator $d_+ = \partial_t - z^2 A \partial_z$, which is the directional derivative along the outgoing null geodesic. At this point, the set of equations (2.4) has the following nested structure

$$\Sigma'' + \frac{2}{z} \Sigma' + \frac{1}{4} \left(\frac{G'^2}{G^2} + \phi'^2 \right) \Sigma = 0, \quad (\text{B.3a})$$

$$F'' + \left(\frac{2}{z} - \frac{G'}{G} \right) F' + \left(\partial_z + \frac{2}{z} - \frac{G'}{G} \right) \left(\frac{2\Sigma'}{\Sigma} - \frac{G'}{G} \right) F = S_F[\phi, G, \Sigma], \quad (\text{B.3b})$$

$$(d_+ \Sigma)' + \frac{\Sigma'}{\Sigma} d_+ \Sigma = S_{d_+ \Sigma}[\phi, G, \Sigma, F], \quad (\text{B.3c})$$

$$(d_+ G)' + \left(\frac{\Sigma'}{\Sigma} - \frac{G'}{G} \right) d_+ G = S_{d_+ G}[\phi, G, \Sigma, F, d_+ \Sigma], \quad (\text{B.3d})$$

$$(d_+ \phi)' + \frac{\Sigma'}{\Sigma} d_+ \phi = S_{d_+ \phi}[\phi, G, \Sigma, F, d_+ \Sigma], \quad (\text{B.3e})$$

$$A'' + \frac{2}{z} A' = S_A[\phi, G, \Sigma, F, d_+ \Sigma, d_+ G, d_+ \phi], \quad (\text{B.3f})$$

$$(d_+ F)' - \left(\frac{2\Sigma'}{\Sigma} + \frac{G'}{G} \right) d_+ F = S_{d_+ F}[\phi, G, \Sigma, F, d_+ \Sigma, d_+ G, d_+ \phi, A], \quad (\text{B.3g})$$

$$d_+ d_+ \Sigma = S_{d_+ d_+ \Sigma}[\phi, G, \Sigma, F, d_+ \Sigma, d_+ G, d_+ \phi, A, d_+ F], \quad (\text{B.3h})$$

where the prime stands for the derivative with respect to the variable z . Once given the data for the fields ϕ and G on the time slice t_0 , the above equations can be solved sequentially, since the source terms given in the right-hand side of the equations depends only on the known fields. In fact, the last two equations are not solved but used to detect numerical errors. The reason this can be done is that once the field A is solved from the equation (B.3f), the fields ϕ and G can be pushed to the next time slice $t_0 + dt$ by integrating in time for $\partial_t \phi$ and $\partial_t G$, which can be obtained from the auxiliary fields

$$\partial_t \phi = d_+ \phi + z^2 A \phi', \quad (\text{B.4a})$$

$$\partial_t G = d_+ G + z^2 A G'. \quad (\text{B.4b})$$

The procedure is iterated until the entire simulation is completed.

B.2 Boundary conditions

In order to clarify the boundary conditions, we expand the field equations (B.3) near the AdS boundary and obtain the asymptotic behavior of the fields as follows

$$\phi = \phi_1 z + \phi_2 z^2 + o(z^3), \quad (\text{B.5a})$$

$$G = 1 + g_3 z^3 + o(z^4), \quad (\text{B.5b})$$

$$\Sigma = z^{-1} + \lambda - \frac{\phi_1^2}{8} z + o(z^2), \quad (\text{B.5c})$$

$$F = -\partial_x \lambda + f_1 z + o(z^2), \quad (\text{B.5d})$$

$$A = \frac{1}{2} z^{-2} + \lambda z^{-1} + \frac{1}{2} \lambda^2 - \frac{\phi_1^2}{8} - \partial_t \lambda + a_1 z + o(z^2), \quad (\text{B.5e})$$

where the source of the scalar field ϕ_1 is a free parameter for the field equations, which is used to quench the system in our work. Since the asymptotic behavior of the fields is known, the scalar operator and energy momentum tensor operator can be evaluated immediately from the equations (2.5)

$$\langle O \rangle = \frac{1}{2} (\lambda \phi_1 + \phi_2 - \partial_t \phi_1), \quad (\text{B.6a})$$

$$\langle T_{ij} \rangle = \begin{pmatrix} -2a_1 - \phi_1 \langle O \rangle & -\frac{3}{2} f_1 + \frac{1}{4} \phi_1 \partial_x \phi_1 & 0 \\ -\frac{3}{2} f_1 + \frac{1}{4} \phi_1 \partial_x \phi_1 & -a_1 + \frac{3}{2} g_3 & 0 \\ 0 & 0 & -a_1 - \frac{3}{2} g_3 \end{pmatrix}. \quad (\text{B.6b})$$

Meanwhile, the Ward-Takahashi identity (2.8) gives rise to the time derivatives of a_1 and f_1 as follows

$$\partial_t a_1 = \frac{3}{4} \partial_x f_1 - \frac{1}{2} \phi_1 \partial_t \langle O \rangle - \frac{1}{8} (\partial_x \phi_1)^2 - \frac{1}{8} \phi_1 \partial_x^2 \phi_1, \quad (\text{B.7a})$$

$$\partial_t f_1 = \frac{2}{3} \partial_x a_1 - \partial_x g_3 + \frac{2}{3} \partial_x \phi_1 \langle O \rangle + \frac{1}{6} \partial_t \phi_1 \partial_x \phi_1 + \frac{1}{6} \phi_1 \partial_x \partial_t \phi_1. \quad (\text{B.7b})$$

Actually, the above equations can also be obtained by asymptotic analysis of equations (B.3g) and (B.3h) on the boundary, respectively.

With these preliminaries in hand, we can now start discussing how to solve these equations (B.3). First, the equation (B.3a) is a linear second order ordinary differential equation for the field Σ . The two integration constants are fixed by the coefficients of the first and second terms in the asymptotic behavior (B.5c), which indicates the parameter λ must be considered as the dynamical variable like ϕ and G . The corresponding time derivative term can be extracted from the asymptotic behavior of field A (B.5e)

$$\partial_t \lambda = \lim_{z \rightarrow 0} \left(\frac{1}{2} z^{-2} + \lambda z^{-1} + \frac{1}{2} \lambda^2 - \frac{\phi_1^2}{8} - A \right). \quad (\text{B.8})$$

Second, the coefficient of the subleading term f_1 in the asymptotic behavior of field F (B.5d) provides the single integration constant for the equation (B.3b) due to the vanishing coefficient of the z^{-2} term. The value of its time derivative can be easily calculated from equation (B.7b). Then, the apparent horizon condition is used to fix the single needed integration constant for the equation (B.3c)

$$d_+ \Sigma(z_h, t, x) = \frac{1}{2G\Sigma} \left(\frac{z^2 F^2 \Sigma'}{\Sigma} + \frac{F \partial_x G}{G} - \partial_x F \right) \Big|_{z_h}. \quad (\text{B.9})$$

Next, for the equations (B.3d) and (B.3e), the integration constants are fixed by the coefficients of the first term in the asymptotic behavior $d_+ G \sim -\frac{3}{2} g_3 z^2 + o(z^3)$ and the second term in the asymptotic behavior $d_+ \phi \sim -\frac{1}{2} \phi_1 - (\lambda \phi_1 + \phi_2 - \partial_t \phi_1) z + o(z^2)$, respectively. As we said before, we require the position of the apparent horizon is time invariant, meaning that the time derivative of the condition (B.9) is also always satisfied at the apparent horizon. Using the equation (B.3h), the stationary horizon condition can induce a second order elliptic equation for A at the horizon, which fixes one of the two integration constants. The other is fixed by the coefficient of the leading term in the asymptotic behavior (B.5e). The numerical code is freely available at <https://github.com/QianChen2022/HFOPT>.

B.3 Convergence test

In our integration strategy, the redundant boundary condition (B.7a) induced by equation (B.3h) on the AdS boundary allows us to detect numerical errors during the evolution. Without loss of generality, we take the case of spontaneous dynamical transition in Fig. 2(a) as an example to demonstrate the accuracy and convergence of our numerical code. At this time, the condition (B.7a) is exactly the energy conservation condition $\partial_t \bar{E} = 0$ due to the time-independent scalar source. Since the homogeneous state as the initial data is obtained by the Newton-Raphson iteration algorithm, in order to avoid the influence of the iterative error, we keep the number of grid points along the radial direction (z) and vary the number of grid points along the spatial direction (x). Due to the spectral method, the expected convergence rate is exponential. The results in Fig. 8 show that the accuracy of our numerical code improves exponentially as the grid points increase, which is exactly the spectral accuracy.

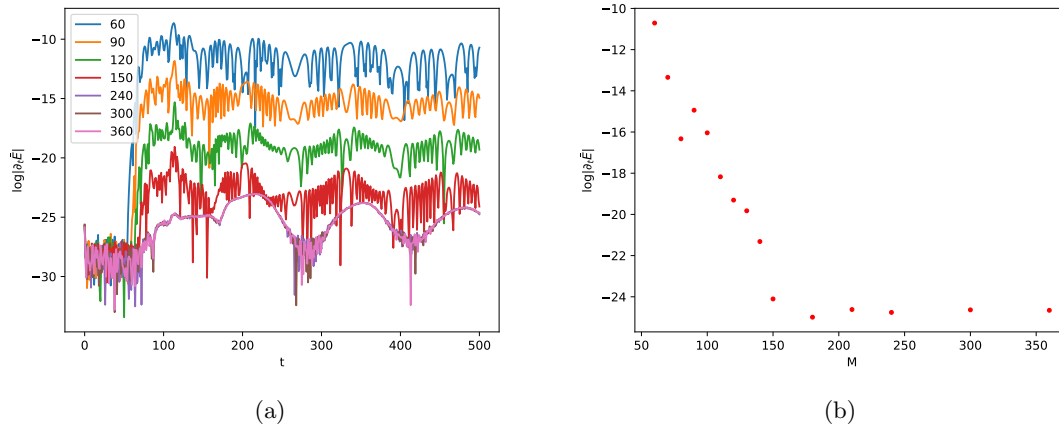


Figure 8. The accuracy and convergence of our numerical code during the spontaneous dynamical transition in Fig. 2(a). (a): The value of $\log|\partial_t \bar{E}|$ as a function of time with different numbers of grid points along the spatial direction. (b): The value of $\log|\partial_t \bar{E}|$ at $t = 500$ varies with the numbers of grid points along the spatial direction.

Acknowledgement

This research is partly supported by National Key Research and Development Program of China Grant No. 2021YFC2203001 and the Natural Science Foundation of China (NSFC) under Grant Nos. 11731001, 11975235, 12035016, 12075026, 12275350 as well as by China Postdoctoral Science Foundation, under the National Postdoctoral Program for Innovative Talents BX2021303.

References

- [1] J. M. Maldacena. The Large N limit of superconformal field theories and supergravity. *Adv. Theor. Math. Phys.*, 2:231–252, 1998.
- [2] S. S. Gubser, I. R. Klebanov, and A. M. Polyakov. Gauge theory correlators from noncritical string theory. *Phys. Lett. B*, 428:105–114, 1998.
- [3] E. Witten. Anti-de Sitter space and holography. *Adv. Theor. Math. Phys.*, 2:253–291, 1998.
- [4] E. Witten. Anti-de Sitter space, thermal phase transition, and confinement in gauge theories. *Adv. Theor. Math. Phys.*, 2:505–532, 1998.
- [5] P. M. Chesler and L. G. Yaffe. Numerical solution of gravitational dynamics in asymptotically anti-de Sitter spacetimes. *JHEP*, 07:086, 2014.
- [6] S. S. Gubser and A. Nellore. Mimicking the QCD equation of state with a dual black hole. *Phys. Rev. D*, 78:086007, 2008.
- [7] Ó. J. C. Dias, J. E. Santos, and B. Way. Localised and nonuniform thermal states of super-Yang-Mills on a circle. *JHEP*, 06:029, 2017.

- [8] R. A. Janik, J. Jankowski, and H. Soltanpanahi. Nonequilibrium Dynamics and Phase Transitions in Holographic Models. *Phys. Rev. Lett.*, 117(9):091603, 2016.
- [9] R. A. Janik, J. Jankowski, and H. Soltanpanahi. Quasinormal modes and the phase structure of strongly coupled matter. *JHEP*, 06:047, 2016.
- [10] U. Gürsoy, A. Jansen, and W. van der Schee. New dynamical instability in asymptotically anti-de Sitter spacetime. *Phys. Rev. D*, 94(6):061901, 2016.
- [11] M. Attems, Y. Bea, J. Casalderrey-Solana, D. Mateos, M. Triana, and M. Zilhão. Holographic Collisions across a Phase Transition. *Phys. Rev. Lett.*, 121(26):261601, 2018.
- [12] M. Attems, Y. Bea, J. Casalderrey-Solana, D. Mateos, M. Triana, and M. Zilhão. Phase Transitions, Inhomogeneous Horizons and Second-Order Hydrodynamics. *JHEP*, 06:129, 2017.
- [13] R. A. Janik, J. Jankowski, and H. Soltanpanahi. Real-Time dynamics and phase separation in a holographic first order phase transition. *Phys. Rev. Lett.*, 119(26):261601, 2017.
- [14] L. Bellantuono, R. A. Janik, J. Jankowski, and H. Soltanpanahi. Dynamics near a first order phase transition. *JHEP*, 10:146, 2019.
- [15] M. Attems, Y. Bea, J. Casalderrey-Solana, D. Mateos, and M. Zilhão. Dynamics of Phase Separation from Holography. *JHEP*, 01:106, 2020.
- [16] M. Attems. Holographic approach of the spinodal instability to criticality. *JHEP*, 08:155, 2021.
- [17] Y. Bea, Ó. J. C. Dias, T. Giannakopoulos, D. Mateos, M. Sanchez-Garitaonandia, J. E. Santos, and M. Zilhão. Crossing a large- N phase transition at finite volume. *JHEP*, 02:061, 2021.
- [18] Y. Bea, J. Casalderrey-Solana, T. Giannakopoulos, D. Mateos, M. Sanchez-Garitaonandia, and M. Zilhão. Domain Collisions. *arXiv: 2111.03355*.
- [19] Y. Bea, J. Casalderrey-Solana, T. Giannakopoulos, A. Jansen, D. Mateos, M. Sanchez-Garitaonandia, and M. Zilhão. Holographic Bubbles with Jecco: Expanding, Collapsing and Critical. 2 2022.
- [20] R. A. Janik, M. Jarvinen, H. Soltanpanahi, and J. Sonnenschein. Perfect Fluid Hydrodynamic Picture of Domain Wall Velocities at Strong Coupling. *Phys. Rev. Lett.*, 129(8):081601, 2022.
- [21] Q. Chen, Y. Liu, Y. Tian, B. Wang, C. Zhang, and H. Zhang. Critical Dynamics in Holographic First-Order Phase Transition. 9 2022.
- [22] C. R. Evans and J. S. Coleman. Observation of critical phenomena and selfsimilarity in the gravitational collapse of radiation fluid. *Phys. Rev. Lett.*, 72:1782–1785, 1994.
- [23] T. Koike, T. Hara, and S. Adachi. Critical behavior in gravitational collapse of radiation fluid: A Renormalization group (linear perturbation) analysis. *Phys. Rev. Lett.*, 74:5170–5173, 1995.
- [24] P. Bizon and T. Chmaj. Critical collapse of Skyrmsions. *Phys. Rev. D*, 58:041501, 1998.
- [25] C. Gundlach and J. M. Martin-Garcia. Critical phenomena in gravitational collapse. *Living Rev. Rel.*, 10:5, 2007.
- [26] C. Zhang, Q. Chen, Y. Liu, W. Luo, Y. Tian, and B. Wang. Critical Phenomena in Dynamical Scalarization of Charged Black Holes. *Phys. Rev. Lett.*, 128(16):161105, 2022.

- [27] C. Zhang, Q. Chen, Y. Liu, W. Luo, Y. Tian, and B. Wang. Dynamical transitions in scalarization and descalarization through black hole accretion. *Phys. Rev. D*, 106(6):L061501, 2022.
- [28] Y. Liu, C. Zhang, Q. Chen, Z. Cao, Y. Tian, and B. Wang. The critical scalarization and descalarization of black holes in a generalized scalar-tensor theory. *arXiv: 2208.07548*.
- [29] G. W. Gibbons and S. W. Hawking. Action Integrals and Partition Functions in Quantum Gravity. *Phys. Rev. D*, 15:2752–2756, 1977.
- [30] M. Bianchi, D. Z. Freedman, and K. Skenderis. Holographic renormalization. *Nucl. Phys. B*, 631:159–194, 2002.
- [31] H. Elvang and M. Hadjiantonis. A Practical Approach to the Hamilton-Jacobi Formulation of Holographic Renormalization. *JHEP*, 06:046, 2016.
- [32] Ó. J. C. Dias, J. E. Santos, and B. Way. Numerical Methods for Finding Stationary Gravitational Solutions. *Class. Quant. Grav.*, 33(13):133001, 2016.
- [33] M. J. Bhaseen, J. P. Gauntlett, B. D. Simons, J. Sonner, and T. Wiseman. Holographic Superfluids and the Dynamics of Symmetry Breaking. *Phys. Rev. Lett.*, 110(1):015301, 2013.
- [34] X. Bai, B. Lee, L. Li, J. Sun, and H. Zhang. Time Evolution of Entanglement Entropy in Quenched Holographic Superconductors. *JHEP*, 04:066, 2015.
- [35] Q. Chen, Z. Ning, Y. Tian, B. Wang, and C. Zhang. Descalarization by Quenching Charged Hairy Black Hole in asymptotically AdS spacetime. 10 2022.
- [36] T. Takayanagi. Holographic Dual of BCFT. *Phys. Rev. Lett.*, 107:101602, 2011.
- [37] M. Nozaki, T. Takayanagi, and T. Ugajin. Central Charges for BCFTs and Holography. *JHEP*, 06:066, 2012.
- [38] A. Almheiri, R. Mahajan, J. Maldacena, and Y. Zhao. The Page curve of Hawking radiation from semiclassical geometry. *JHEP*, 03:149, 2020.
- [39] A. Almheiri, N. Engelhardt, D. Marolf, and H. Maxfield. The entropy of bulk quantum fields and the entanglement wedge of an evaporating black hole. *Journal of High Energy Physics*, 2019(12):1–47, 2019.
- [40] A. Almheiri, R. Mahajan, and J. Maldacena. Islands outside the horizon. *arXiv:1910.11077*, 10 2019.
- [41] A. Almheiri, R. Mahajan, and J. E. Santos. Entanglement islands in higher dimensions. *SciPost Phys.*, 9(1):001, 2020.
- [42] Y. Ling, Y. Liu, and Z. Xian. Island in Charged Black Holes. *JHEP*, 03:251, 2021.
- [43] Y. Ling, P. Liu, Y. Liu, C. Niu, Z. Xian, and C. Zhang. Reflected entropy in double holography. *JHEP*, 02:037, 2022.
- [44] Y. Liu, Z. Xian, C. Peng, and Y. Ling. Black holes entangled by radiation. *JHEP*, 09:179, 2022.
- [45] G. Fu, X. Wang, P. Liu, D. Zhang, X. Kuang, and J. Wu. A novel holographic quantum phase transition and butterfly velocity. *JHEP*, 04:148, 2022.
- [46] G. Fu, H. Gong, P. Liu, X. Kuang, and J. Wu. Charge transport properties in a novel holographic quantum phase transition model. 8 2022.

- [47] P. Liu and J. Wu. Mixed state entanglement and thermal phase transitions. *Phys. Rev. D*, 104(4):046017, 2021.
- [48] Y. Ling, P. Liu, and J. Wu. Characterization of Quantum Phase Transition using Holographic Entanglement Entropy. *Phys. Rev. D*, 93(12):126004, 2016.
- [49] Y. Ling, P. Liu, C. Niu, J. Wu, and Z. Xian. Holographic Entanglement Entropy Close to Quantum Phase Transitions. *JHEP*, 04:114, 2016.
- [50] S. Ryu and T. Takayanagi. Holographic derivation of entanglement entropy from AdS/CFT. *Phys. Rev. Lett.*, 96:181602, 2006.
- [51] H. Casini, M. Huerta, and R. C. Myers. Towards a derivation of holographic entanglement entropy. *JHEP*, 05:036, 2011.
- [52] V. E. Hubeny, M. Rangamani, and T. Takayanagi. A Covariant holographic entanglement entropy proposal. *JHEP*, 07:062, 2007.
- [53] S. Ryu and T. Takayanagi. Aspects of Holographic Entanglement Entropy. *JHEP*, 08:045, 2006.
- [54] A. R. Brown, D. A. Roberts, L. Susskind, B. Swingle, and Y. Zhao. Holographic Complexity Equals Bulk Action? *Phys. Rev. Lett.*, 116(19):191301, 2016.
- [55] M. Alishahiha. Holographic Complexity. *Phys. Rev. D*, 92(12):126009, 2015.
- [56] D. Carmi, S. Chapman, H. Marrochio, R. C. Myers, and S. Sugishita. On the Time Dependence of Holographic Complexity. *JHEP*, 11:188, 2017.
- [57] A. R. Brown, D. A. Roberts, L. Susskind, B. Swingle, and Y. Zhao. Complexity, action, and black holes. *Phys. Rev. D*, 93(8):086006, 2016.
- [58] T. Albash and C. V. Johnson. Evolution of Holographic Entanglement Entropy after Thermal and Electromagnetic Quenches. *New J. Phys.*, 13:045017, 2011.
- [59] H. Liu and S. J. Suh. Entanglement Tsunami: Universal Scaling in Holographic Thermalization. *Phys. Rev. Lett.*, 112:011601, 2014.
- [60] H. Liu and S. J. Suh. Entanglement growth during thermalization in holographic systems. *Phys. Rev. D*, 89(6):066012, 2014.
- [61] B. Chen, W. Li, R. Yang, C. Zhang, and S. Zhang. Holographic subregion complexity under a thermal quench. *JHEP*, 07:034, 2018.
- [62] S. Chapman, H. Marrochio, and R. C. Myers. Holographic complexity in Vaidya spacetimes. Part I. *JHEP*, 06:046, 2018.
- [63] S. Chapman, H. Marrochio, and R. C. Myers. Holographic complexity in Vaidya spacetimes. Part II. *JHEP*, 06:114, 2018.
- [64] Y. Ling, Y. Liu, and C. Zhang. Holographic Subregion Complexity in Einstein-Born-Infeld theory. *Eur. Phys. J. C*, 79(3):194, 2019.
- [65] Y. Ling, Y. Liu, C. Niu, Y. Xiao, and C. Zhang. Holographic Subregion Complexity in General Vaidya Geometry. *JHEP*, 11:039, 2019.
- [66] Y. Ling, Y. Liu, and Z. Xian. Entanglement entropy of an annulus in holographic thermalization. *Chin. Phys. C*, 44(2):023101, 2020.